Journal of Structural Geology, Vol. 4, No. 3, pp. 355 to 372, 1982
Printed in Great Britain

0191-8141/82/030355-18 $03.00/0

A stress-transfer model for the development of extension fracture boudinage

G. E. LLOYD

Centre for Materials Science, University of Birmingham, Birmingham B15 2TT, U.K.

C. C. FERGUSON

Department of Geology, University of Nottingham, Nottingham NG7 2RD, U.K.

K. READING

U.K.A.E.A. (Northern Division), Risley, Cheshire, U.K.

(*Received* 3 *December* 1981; *accepted in revised form* 5 *May* 1982)

Abstract—The term boudinage is used to describe a wide variety of extensional structures in deformed rocks. This paper is mainly concerned with boudinage resulting from through-layer extension fractures followed by separation of the layer segments, thus forming boudins with more or less rectangular cross-sections. In principle, this process is similar to the break up of fibres in fibre-reinforced composite materials extended parallel to the fibre direction. Both processes are controlled by the transfer of stress from the matrix to the fibre (or layer) and a mathematical model for fibre–matrix stress transfer (the 'fibre-loading' model) is well established. We have used this as a basis for developing a stress transfer model for boudinage. The only difference in the basic mathematical formulation results from geometric differences between the two systems; the geometric expressions in the fibre-loading model have, therefore, been rederived for the layer–matrix case.

Stress-transfer theory predicts that the tensile stress in a layer segment rises from a minimum at the end of a segment to a maximum at the centre. This behaviour, which is clearly shown by finite-element models of boudinage structure, suggests that extension fracture boudinage develops by successive 'mid-point' fracturing. According to stress-transfer theory, the process will continue until a layer is reduced to segments (boudins) all of which are shorter than some critical length (for which the tensile fracture strength of the layer is equal to the tensile stress at the mid-point). In practice, successive fracturing will be influenced by two other factors: (1) in nature the controlling material properties (tensile fracture strength, elastic moduli) will not be single-valued but will have a distribution reflecting local variations in lithology and microstructure and (2) major pre-deformation flaws may be present in a layer which will control the 'starting length' of layer segments. These factors are incorporated with the stress-transfer theory into a statistical (Monte Carlo) model for extension fracture boudinage which results in a prediction of boudin aspect ratios. The predicted distribution compares very closely with the observed distribution of 91 quartzite boudins within Lower Carboniferous slates at Tintagel, Cornwall.

The stress-transfer model implies that boudin-defining fractures occur sequentially so that inter-boudin gap lengths will be unequal. Strain estimates based on boudinage structure will vary according to which part and how much of a layer is sampled. A much improved strain estimate is possible based on sequentially closing the inter-boudin gaps. The stress-transfer theory also leads to the possibility of estimating palaeostress from boudinage structure and is the only model available which predicts an aspect ratio distribution of boudins formed by extension fracture. Other than our own, we know of no published data on boudin aspect ratio distributions. Hence, further elaboration of the model is not possible until more field data is available. We hope that our work will encourage the systematic measurement of boudinage as well as the development of alternative models.

INTRODUCTION

THE TERM boudinage was first coined by Lohest (1909) to describe the fragmentation of individual rock layers into 'sausage-shaped' blocks with 'barrel-like' cross-sections which he called boudins. Apart from general descriptions little attention was given to the structure until Cloos (1947) reviewed the literature and suggested possible origins for boudinage. Wilson (1961) suggested a nomenclature for boudinage (Fig. 1a) but this is by no means universally employed and the nomenclature used in this study is shown in Fig. 1(b). The first rigorous mechanical explanation of boudinage structure was by Ramberg (1955) who suggested that of three possible origins — tensile stretching, compression normal to the layer or a stress couple acting at 45° to the layer — only the second could also account for structures in the surrounding matrix. He postulated that layer-normal compression induces flow in the matrix parallel to the layer, which causes tensile stresses to develop in the layer, the magnitude of which are a function of the compressive stress, the rate of elongation, the viscosity ratio between layer and matrix, the frictional strength and area of the interface, and the layer thickness. Using a viscous matrix and elastic-brittle layer analysis, Ramberg derived relationships between the compressive stress, flow-rate, tensile stress magnitude within boudins and size of boudins. These show that the boudin tensile stress depends only on the dimensions (thickness) of the boudin and the pressure gradient in the matrix, while the viscosity ratio controls only the rate of boudinage development.

Since Ramberg's analysis it has been realized that

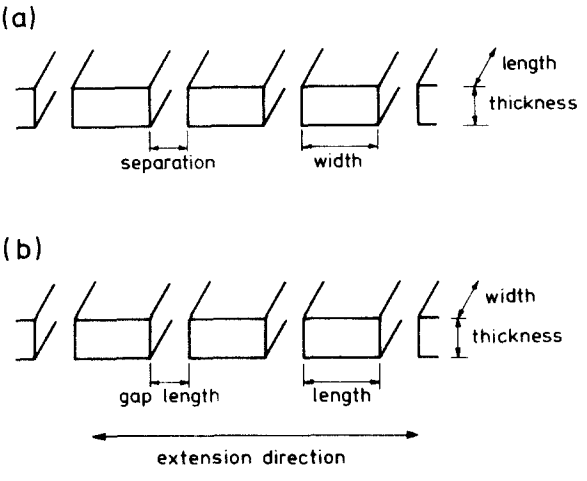

Fig. 1. Boudinage terminologies: (a) after Wilson (1961); (b) this study.

boudinage can develop due to shear fracture (e.g. Gay & Jaeger 1975, Griggs & Handin 1960, Uemura 1965) and that layers below a certain thickness may thin uniformly (Gay & Jaeger 1975, Talbot 1970). Talbot further suggested that layer thickness controlled whether extension or shear fracture occurs.

Ramberg (1955) and Wilson (1961) argued that boudin shape is determined by the characteristics of the layer, with strong brittle layers forming rectangular boudins and more ductile layers forming lenticular boudins. Thus, boudinage should be a useful indicator of relative competence in rocks. However, whereas Ramberg thought that boudinage should also reveal information on the general forces existing during deformation, Wilson considered that only local principal stress directions are indicated.

In spite of these analyses and suggestions that boudinage is a useful indicator of the conditions existing during deformation, the structure has received little attention, although some of the earlier analyses have been verified by computer-modelling techniques (e.g. Stephansson & Berner 1971, Stephansson 1973, Selkman 1978). There have also been several attempts to use boudinage structure in strain analysis, either alone (Schwerdtner 1970) or in conjunction with folded layers or veins (Ramsay 1967, Talbot 1970). Uemura (1965) has argued that shear-fracture boudinage develops at fold hinges while extension-fracture boudinage is confined to limbs and, hence, that boudinage could be useful in recognizing major folds. More recently, Sanderson & Meneilly (1981) have used boudinaged andalusites to determine strain. However, in general, boudinage structure is a rather unpromising finite strain estimator and this may explain why few geologists have given it much attention. Another reason could be that, in spite of the analyses by Ramberg and others, no theory exists for the development of boudinage along a whole layer; previous analyses have concentrated on the formation of individual fractures and boudins.

A structure similar, in many respects, to boudinage is pinch-and-swell which involves ductile flow and necking but no fracturing. Smith (1975, 1977, 1979), in an elegant series of papers, argues that folding and boudinage are related structures (requiring only different orientations of principal stresses) which develop from perturbations at the layer–matrix interfaces. This work makes it clear that viscous layers are much more stable in extension than in shortening and that some non-Newtonian behaviour is essential for a layer to become unstable at all (i.e. to show pinch-and-swell). This helps to explain the rarity of boudinage relative to folding in wholly ductile systems. However, Smith's boudinage is really pinch-and-swell structure with an added assumption (mechanically soundly based) that fracture will tend to occur in the neck regions. He does not consider boudinage in which ductile flow is unimportant. Smith's theories, which are supported by a recent approach by Fullagar (1980) based on vorticity, lead to a prediction that boudin length to thickness ratios (using the terms as in Fig. 1b) should lie between 4 and 6 (his equations are similar to those derived by Ramberg, 1955). This conflicts with Strömgård's (1973) predicted range of from 2 to 4 (with support from natural examples cited by Ekstrom 1975 and Troeng 1975), whereas Talbot (1970) reports values from 2:1 to > 20:1 in natural boudinage.

From the preceding comments it is apparent that boudinage is a complex structure involving brittle and/or ductile deformations. The picture is further complicated by the practice of using the term 'boudinage' to refer to any structure involving fracture and separation. Thus, structures differing widely from each other and from Lohest's original are called boudinage (e.g. rectangular and lozenge shaped boudins, pinch-and-swell, fractured minerals, fossils, pebbles and other such inclusions). The terms 'internal' and 'foliation' boudinage have been applied respectively by Cobbold *et al.* (1971) and Platt & Vissers (1980) to describe boudinage-like structures in homogeneous rock masses that are strongly anisotropic. The term boudinage, therefore, encompasses a wide variety of disparate structures, examples of which are shown in Fig. 2, and consequently, it is highly unlikely that there is one single mechanical origin.

In this contribution, we derive a mechanism for the origin of extension-fracture boudinage, beginning with recent results obtained by Lloyd & Ferguson (1981) from elastic–plastic finite element simulations. These authors established that 'hard' layers (i.e. those with a relatively high flow stress level) fracture to form rectangular boudins, with ductile deformation being restricted to post-fracture modification of the corners; and that further fracture is possible across the centre of any boudin having sufficient length to allow the tensile stress to exceed the fracture strength of the rock (a tendency noted by Ramberg in his original analysis). Similar behaviour is shown by cylindrical fibres of one material enclosed in a matrix of another (Fig. 3a). Such fibre-reinforced composite materials are important in modern technology and their behaviour has been studied in considerable detail. It is our contention that extension-fracture boudinage develops by a stress-transfer mechanism similar to that in the theory of fibre-loading developed to explain the strength of fibre-reinforced composites. In the following

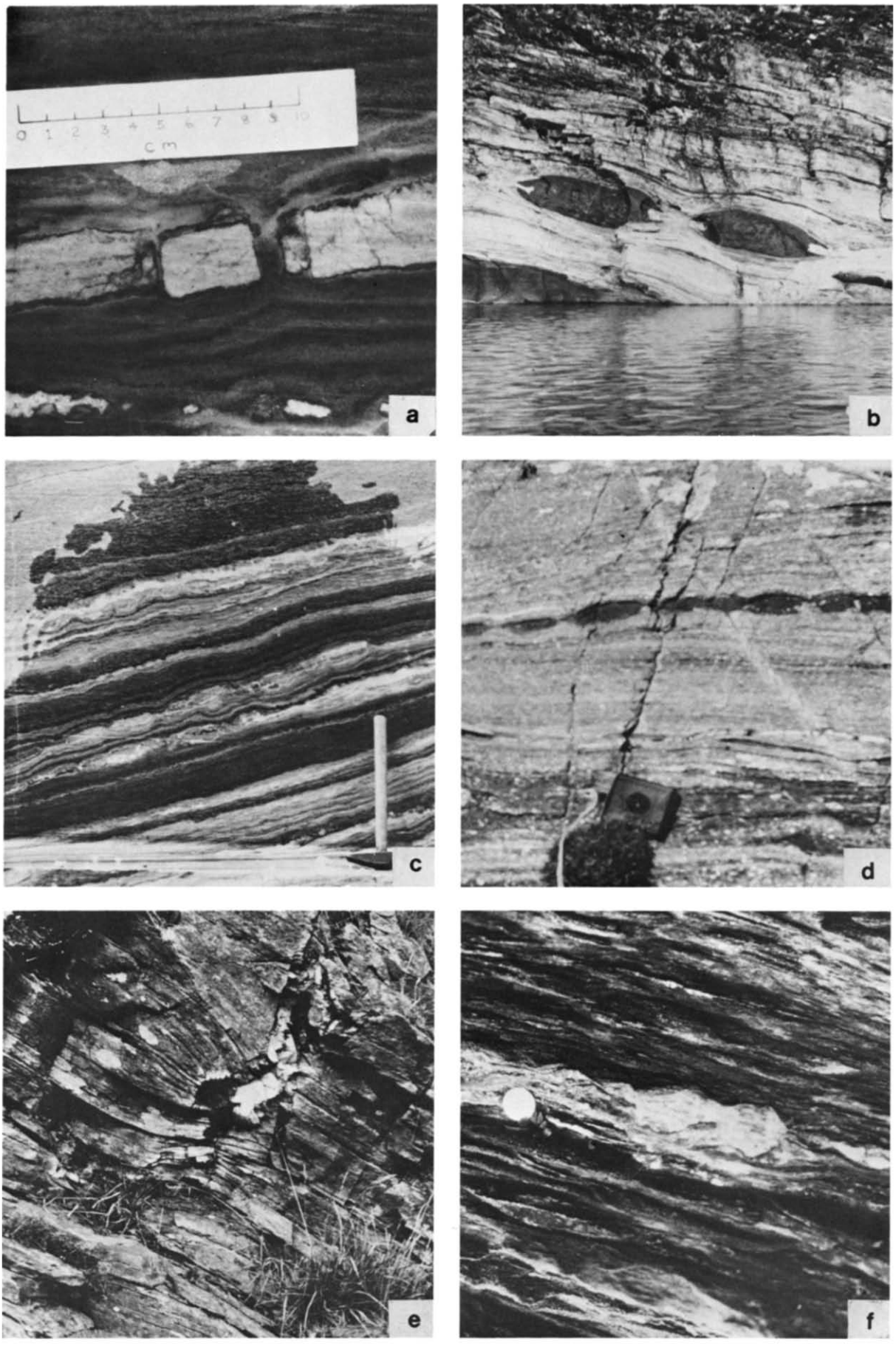

Fig. 2. Examples of different types of boudinage structure. (a) Rectangular boudins caused by layer-normal extension fractures; tremolite layer in impure Dalradian marbles, Streamstown Marble Quarry, Connemara, W. Ireland. (b) Extreme barrel shaped boudins; amphibolite dyke in quartz-feldspathic gneiss, Sermiligaq fjord, East Greenland (photo courtesy of Dr A. E. Wright). (c) Train of boudins with lenticular outlines; serpentinised diopside–tremolite layer in impure Dalradian marbles, Streamstown Marble Quarry, Connemara, W. Ireland. (d) Pinch-and-swell structure (note complete separation of some 'swells' into lenticular boudins); amphibolite layer in Connemara migmatites, Knock Head, W. Ireland. (e) Internal boudinage in foliated Dalradian quartzite (note fracture filled by quartz crystallised from solution); north of Kinloch Rannoch, Perthshire, Scotland. (f) Boudinaged inclusions; dolomite segregations in volcanic slates (note quartz-filled gap); Barras Nose Head, Cornwall, England.

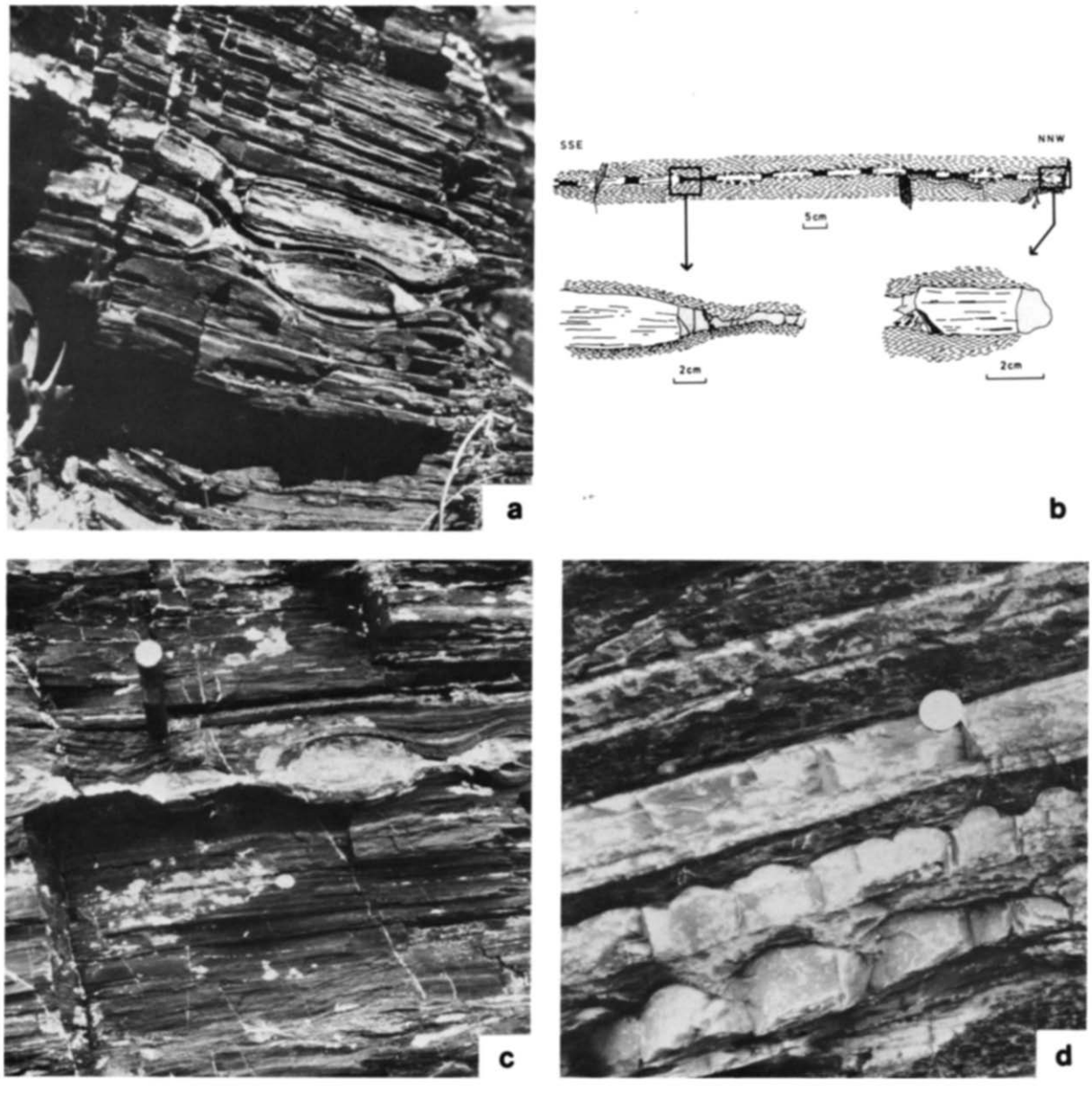

Fig. 7. Structures at Tintagel, Cornwall relevant to the stress-transfer model for the development of extension fracture boudinage. (a) Extension fracture boudinage of thin quartzite layer in Barras Nose Slates; note that the layer-parallel cleavage in the slates curves around the boudins making them appear lenticular rather than rectangular. (b) Tracing of layer shown in (a) illustrating main features; note the rectangular shape of the boudins, and the gaps filled by quartz crystallized from solution. (c) Further example of rectangular extension fracture boudinage of thin quartzite layers in Barras Nose Slates; note that the quartz, crystallized from solution, occupies only the gap regions adjacent to boudin ends, the rest of the inter-boudin gap being filled by matrix. (d) Example of inbuilt flaws in a relatively undeformed layer; load structures in sandstone layer in inverted turbidite sequence at Millook Haven, Cornwall. The frequency of flaws is much greater than that predicted for the Tintagel boudinage.

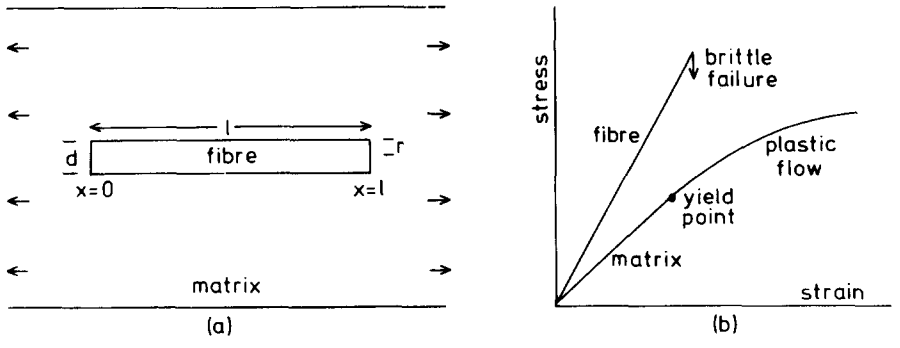

Fig. 3. Fibre-composite materials: (a) system geometry and (b) stress–strain curves.

sections, we outline the main features of this theory and the modifications necessary for it to provide a mathematical model of extension-fracture boudinage.

MECHANICS OF COMPOSITE MATERIALS

Fibre loading

The theory of fibre loading was first outlined by Cox (1952) and developed by Kelly (1973). Consider a composite body, consisting of a single fibre of one material embedded in an isotropic matrix of another, which is extended parallel to the fibre direction (Fig. 3a). If the stress–strain curve of the matrix has a lower gradient than that of the fibre (Fig. 3b) then the matrix, although reinforced by the presence of the fibre, will show the greater displacements. Shear strains form on all planes parallel to the fibre axis and, together with the shear stresses, are responsible for distributing the applied load between the matrix and the fibre (i.e. stress transfer). The distribution of tensile stress in the fibre is given (Kelly 1973, p. 177) by:

$$\sigma = E_f \varepsilon \left[1 - \frac{\cosh\left[\beta(l/2 - x)\right]}{\cosh\left[\beta l/2\right]}\right] \qquad (1)$$

in which,

$$\beta = \left[\frac{2\pi G_m}{E_f A_f \ln(R_0/r)}\right]^{1/2} = \left[\frac{H}{E_f A_f}\right]^{1/2} \qquad (2)$$

with the following notation:

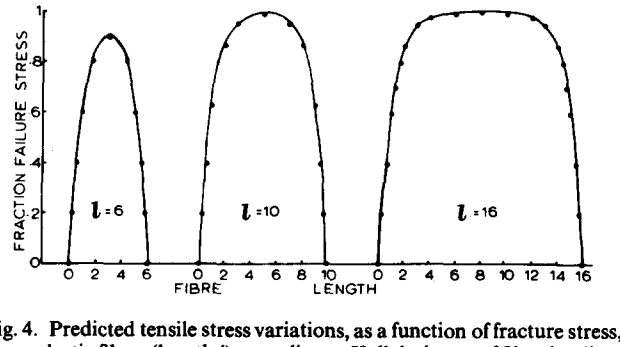

Fig. 4. Predicted tensile stress variations, as a function of fracture stress, along elastic fibres (length l) according to Kelly's theory of fibre-loading.

E_f, Young's modulus of fibre; ε, far field matrix strain; l, fibre length; x, distance from end of fibre ($0 \leqq x \leqq l$); G_m, shear modulus of matrix; A_f, cross-sectional area of the fibre; R_0, mean distance between adjacent fibres and r, fibre radius.

Equation (1) shows that the tensile stress in a fibre builds up from the ends and is a maximum at the centre (Fig. 4). Using this equation, the shear stress τ at the fibre–matrix interface can be determined (Kelly 1973, p. 179) which shows that the maximum values occur at the fibre ends and the minimum value at the centre.

When the tensile stress which is transferred to the fibre exceeds the fibre fracture strength the fibre will break, ideally across its centre where the tensile stress is a maximum. The theory, therefore, predicts a range of fibre segment lengths (Kelly 1973, p. 172, Ohsawa *et al.* 1978),

$$l_c/2 \leqq l \leqq l_c, \qquad (3)$$

where l is the length of broken fibre segments and l_c is the critical length below which the maximum tensile stress cannot exceed the fracture strength; l_c is, therefore, the maximum length of broken fibre possible and, according to Ohsawa *et al.* (1978), is equal to $4\bar{l}/3$, where $\bar{l}$ is the mean length of broken segments.

Geological fibre-loading

In the development of mylonitic microstructure in polyminerallic rocks some minerals (e.g. quartz) behave in a plastic manner while others (e.g. feldspars) behave in a more brittle manner. The specific behaviour of brittle minerals may depend on whether there has been any prior plastic deformation (White *et al.* 1980); minerals which have suffered a limited amount of plastic deformation (e.g. plagioclase, amphibole) commonly show shear fractures (Allison & Latour 1977), but those which do not show any evidence of plastic deformation often have extension fractures sometimes accompanied by separation of the segments. White *et al.* (1980) compare this behaviour with similar features in deformed metals and propose two mechanisms for the fracturing process: (1) 'fibre-loading', which we have described above and shall return to later and (2) the pile-up of dislocations at points along mineral–matrix boundaries, discussed in detail by Mitra (1978). While the first mechanism predicts a relatively narrow range of segment lengths, the second does not

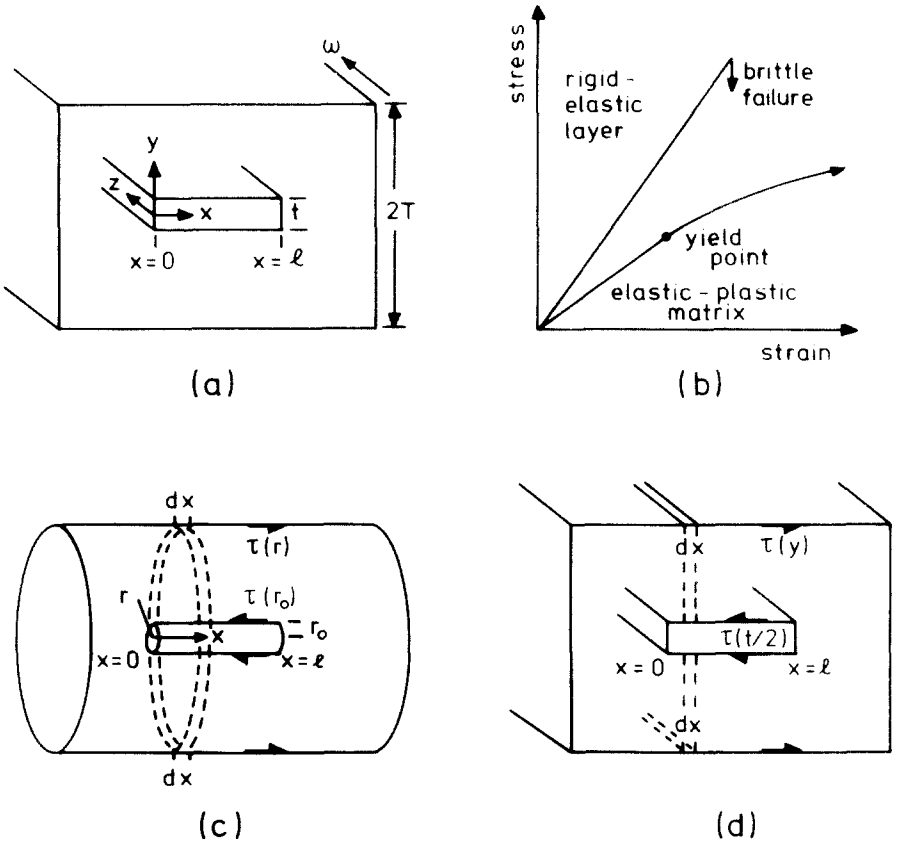

Fig. 5. Layer-composite materials: (a) system geometry; (b) stress–strain curves; (c) shear stress in a fibre composite and (d) shear stress in a layer composite.

favour any particular length and, hence, the two mechanisms should be distinguishable. Watts & Williams (1980) have proposed that feldspars in a granitoid mylonite from the North Armorican shear zone have fractured by a fibre-loading process, but Boullier (1980) has suggested, on the evidence of fractured feldspars in a granulite mylonite from the Pan-African mobile belt, that although fibre-loading may occur initially it may not persist to large strains.

The geometric configuration of brittle minerals in a ductile matrix is very similar to that of fibre composite materials and it is perhaps not surprising that they should show similar behaviours. The extension-fracture boudinage of a rock layer is much less similar and we must, therefore, justify the application of the 'fibre-loading' model to this structure. In the next section, we derive an analogous theory for layer–matrix systems.

Layer–matrix systems

Consider a composite body, consisting of a single-layer segment embedded in an isotropic matrix, which is extended parallel to the x-direction (Fig. 5a). Initially we shall assume elastic material properties. We now need to know how the load is transferred to the layer in order for brittle fracture to occur.

Transfer of stress. In the system shown in Fig. 5(a), elastic displacements in the x direction are different for the layer and the matrix due to their different material properties. Just as in the fibre–matrix system, shear strains form on all planes parallel to the layer and, together with the shear stresses, are responsible for distributing the load between the matrix and the layer. If the matrix stress–strain curve has a lower gradient than that of the layer then the matrix will show the greater displacements (Fig. 5b) but will be reinforced by the layer. We assume that overall the matrix deforms more or less homogeneously but that locally the uniform stress–strain state is perturbed by load transfer to the layer. In any reinforced system (whether fibre–matrix or layer–matrix) it is reasonable to assume (Cox 1952) that the load P in the reinforcing material varies with distance x (from either end) according to

$$\frac{dP}{dx} = H(u - v). \tag{4}$$

For a layer-matrix system u is the longitudinal displacement in the layer and v is the corresponding displacement the matrix would undergo if the layer was absent. H is a constant, the value of which depends on the system geometry and the elastic moduli. Hence, by analogy with equation (1) and using subscript s to denote a layer (or slab), the distribution of tensile stress in the layer is

$$\sigma = E_s \varepsilon \left[1 - \frac{\cosh [\beta(l/2 - x)]}{\cosh [\beta l/2]} \right]. \quad (5)$$

This equation is derived by recognizing that

$$P = E_s A_s \frac{du}{dx}, \quad (6a)$$

$$\frac{dv}{dx} = \varepsilon = \text{constant}. \quad (6b)$$

Differentiating equation (4) and substituting equation (6) yields,

$$\frac{d^2P}{dx^2} = H \left[\frac{P}{E_s A_s} - \varepsilon \right],$$

which can be solved (Kelly 1973, p. 177) to give

$$P = E_s A_s \varepsilon + Q \sinh(\beta x) + S \cosh(\beta x), \quad (7)$$

where Q and S are constants. The variable

$$\beta = (H/E_s A_s)^{1/2}$$

incorporates all the relevant geometric properties of the system. At the ends of the layer $P = 0$ and the distribution of tensile stress in the layer is given by equation (5) using $\sigma = P/A_s$. We now need to derive an expression for β analogous to equation (2). For a fibre–matrix system the shear stress $\tau(r)$ in the direction of the fibre axis acting on planes parallel to the axis affects, in the limit dx, the circumference of a circle, radius r, centered on the fibre axis (Fig. 5c). In contrast in the layer–matrix system the shear stress acts on two surfaces distance $\pm y$ from the layer (Fig. 5d), i.e. 2wdx. Thus, for a fibre-matrix system $dP/dx = -2\pi r\tau(r)$ (Kelly 1973, p. 178) but for a layer matrix system,

$$\frac{dP}{dx} = -2w\tau(y). \quad (8)$$

Combining equations (4) and (8),

$$H = -2w\tau(y)/(u - v). \quad (9)$$

If c is the actual displacement in the matrix close to the layer then at the layer–matrix interface $c = u$ (assuming no slippage) while at a distance from the layer equal to y, $c = v$. For mechanical equilibrium of the infinitesimal matrix section, thickness dx, perpendicular to the layer (Fig. 5d) the shear forces at the layer–matrix interface and at a distance y from the layer must be equal and opposite, i.e.

$$-(2w\mathrm{d}x)\,\tau(y) = \text{const.} = -(2w\mathrm{d}x)\,\tau\,(t/2). \quad (10)$$

In the case of a cylindrical fibre, the area over which the shear stress acts varies with radial distance from the fibre (Fig. 5c) but in the layer case this area is constant (Fig. 5d). The shear strain in the matrix can be written,

$$\frac{dc}{dy} = \frac{\tau(y)}{G_m} = \frac{\tau(t/2)}{G_m} \quad (11)$$

in which case integration of the shear displacements over the ranges $(t/2, y)$ and $-(t/2, y)$ yields

$$\Delta c = 2 \int_{t/2}^{y} \frac{\tau(t/2)}{G_m} dy = \frac{2\tau(t/2)}{G_m}(y - t/2). \quad (12)$$

However, $\Delta c = (v - u)$ by definition, and so from equation (9),

$$H = w\tau(t/2)\frac{G_m}{\tau(t/2)(y - t/2)} = wG_m/(y - t/2). \quad (13)$$

By analogy with equation (2) and remembering that $A_s = tw$, we have

$$\beta = \left[\frac{G_m}{E_s} \frac{1}{(y - t/2)t} \right]^{1/2}. \quad (14)$$

The rate of increase of stress from the ends to the centre of a layer depends on the value of G_m/E_s and as expected the maximum stress occurs across the centre of the layer. Similarly, maximum values of shear stress occur at the layer ends with a minimum at the centre. Having considered how stress is transferred from matrix to layer in an all-elastic system and shown that it is basically the same as that for the fibre–matrix system we can now incorporate this into an analysis of layer fracture.

Layer fracture. If the tensile and shear stresses which are transmitted from the matrix to the layer exceed the local fracture stress then the layer will fracture. For a layer of thickness t the maximum increment of stress $d\sigma$ produced in length dx is equal to the force exerted by the shear stress, which in turn is given by the product of the shear stress and the interfacial area ($2w$ dx τ) divided by the cross-sectional area (wt),

$$\frac{d\sigma}{dx} = \frac{2\tau}{t}. \quad (15)$$

Integration of this expression shows that the ultimate fracture stress of the layer, σ_{uf}, occurs at a distance $t\sigma_{uf}/2\tau$ from the layer ends. The maximum length of layer segment possible (i.e. the critical segment length) is, therefore, $t\sigma_{uf}/\tau = l_c$ since segments longer than this will fracture. There is also a minimum segment length, $t\sigma_{uf}/2\tau = l_c/2$, since segments shorter than the critical length cannot fracture further. The range of layer-segment lengths, l, is therefore,

$$t\sigma_{uf}/2\tau \leqq l \leqq t\sigma_{uf}/\tau. \quad (16)$$

Now Ohsawa *et al.* (1978) argue that, for fibre fracture, the lengths of broken segments should be uniformly distributed within the permitted range so that, from inequality (16), we might expect the mean length of segment, $\bar{l}$, to be

$$\bar{l} = \left(\frac{t\sigma_{uf}}{2\tau} + \frac{t\sigma_{uf}}{\tau} \right) \frac{1}{2} = \frac{3}{4} \frac{t\sigma_{uf}}{\tau} = \frac{3}{4} l_c. \quad (17)$$

However, experiments by Ohsawa *et al.* (1978) showed that fibre lengths are almost normally distributed between the predicted limits. Nevertheless, by calculating the mean boudin length, the critical length can still be estimated from equation (17) and hence $2\bar{l}/3 \leqq l \leqq 4\bar{l}/3$.

Plastic matrix behaviour. If the matrix deforms plastically then, as the load is applied, the different displacements in matrix and layer will result in shear stresses in the matrix, close to the layer ends, in excess of those due only to the applied stress. The predicted variation of shear stress with load for fibre–matrix systems is shown in Fig. 6(a). From the stress-transfer analysis the variation for a layer–matrix system should be of similar form. At small loads P_1 (such that $\tau_{max} < \tau_y$, the shear yield stress of the matrix) the shear stress at the layer–matrix interface is determined by the elastic behaviour of the matrix. At higher loads (e.g. P_2) plastic deformation occurs in the matrix, initially near the layer segment ends ($x < a$ in Fig. 6a). This limits the maximum shear stress to τ_y ($\simeq \sigma_y/2$), the shear yield stress of the matrix, which in turn limits the maximum value of the elastic matrix strain to σ_y/E; for distances $x > a$ away from the layer segment ends, the shear stress decreases as before.

The general effects of matrix plasticity on the tensile stress distribution in a fibre (or layer) are illustrated in Fig. 6(b). If $\tau_{max} < \tau_y$ (e.g. load P_1) the distribution of tensile stress is as previously described for the all-elastic system. However, when the load (e.g. P_2) is sufficient to cause yield in the matrix near the ends of a layer segment (say, $x < a$) the longitudinal strain within the layer is substantially different from that just outside the layer. The constant shear stress ($\tau = \tau_y$) in the plastically-deforming matrix causes a steep (and, from equation 15, a linear) increase in the tensile stress within the layer, while beyond the region of matrix plasticity ($x > a$) the extra tensile stress is elastically transferred as before. As more of the matrix deforms plastically, a correspondingly greater proportion of the layer is affected by the linear increase in tensile stress until, eventually, the ultimate fracture stress, σ_{uf}, may be reached midway between the layer ends (case P_3 in Fig. 6b.). However, if the maximum tensile stress in the layer is less than σ_{uf} even when all the adjacent matrix has yielded (case P_4), fracture is only possible if further load is applied thus increasing the shear stress and, therefore, the gradient $d\sigma/dx$ (case P_5).

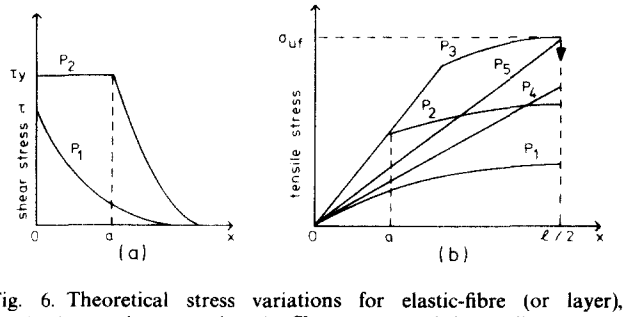

Fig. 6. Theoretical stress variations for elastic-fibre (or layer), plastic–matrix composites. (a) Shear stress and (b) tensile stress.

Finite element simulations of boudinage

Support for the stress transfer theory for layer-matrix systems comes from elastic–plastic finite-element simulations (FEM) of boudinage; for a detailed description of this approach see Lloyd & Ferguson (1981). The results of these simulations show that the main features of boudinage are largely determined by the gradients of the stress–strain curves for the boudin and matrix and by the amount of deformation. However, since the simulations are restricted to the post-fracture modification of rectangular boudins formed by an (assumed) extension fracture, they do not account for the development of boudinage along an entire layer. Nevertheless the distributions of stresses and strains within and adjacent to boudins determined by these simulations are very similar to those predicted by the stress-transfer model. The least compressive stress values occur midway between layer/boudin ends which suggest that further fracture is most likely half way between the sites of earlier fractures. Furthermore, the simulations show that yield occurs first within the matrix adjacent to the corners of boudins, as predicted by the theory, and that gross variations in stress and strain are restricted to the end of the boudins, the central regions having nearly uniform values. Differences between the finite element simulations and the stress transfer theory are minor and arise because the former contain no fracture criterion which would tend to limit the values of the stresses and strains.

Implications for natural boudinage

The close similarity between the FEM simulations and the modified theory of fibre loading suggests to us that stress transfer is a possible mechanism for the development of extension fracture boudinage. It is worth mentioning that since axisymmetric FEM analyses of cylindrical fibre composites by Agarwal *et al.* (1974) are very similar to those presented here, then the difference in geometry between the two systems has very little effect on the qualitative behaviour.

Before considering some natural examples it is worth discussing some of the implications of a stress-transfer model for boudinage. Stress transfer requires that fracture, separation and, if the layers are able to deform plastically, ductile deformation, occur simultaneously at different parts of the layer. The break up of a layer by extension fracture is not a single event but occurs sequentially so long as the boudins are long enough for the deviatoric tensile stress across their centre to exceed the fracture strength of the rock. Thus, inter-boudin gap lengths will not be equal, early fracture sites being indicated by larger gaps than later ones. Strain estimates based on boudinage should take into account the sequential development of the structure (Ferguson 1981). Ductile matrix deformation is aided by the presence of boudins, especially close to boudin corners which act as local stress raisers enabling the yield stress to be exceeded more readily.

COMPARISONS WITH NATURAL BOUDINAGE

The stress-transfer theory derived above predicts that the length distribution of boudins resulting from extension fracture boudinage of a layer is constrained by a critical boudin length l_c. This length is the shortest length of layer segment which can fracture because, in shorter segments, the tensile stress nowhere exceeds the tensile strength of the layer. Therefore, in natural boudinage formed by a stress-transfer type mechanism, the distribution of boudin length/thickness (aspect) ratios should be predictable. In this section, we explore this possibility by comparing the model predictions with measurements of 91 boudins from Tintagel, Cornwall.

General geology

The rocks at Tintagel are Upper Devonian and Lower Carboniferous slates and phyllites (McKeown *et al.* 1973) which display a strong penetrative cleavage, in the main subhorizontal and parallel to bedding (Fig. 7a). The detailed interpretation of the structural geology is still the subject of much debate (cf. Wilson 1951, Freshney *et al.* 1972, Sanderson & Dearman 1973, Hobson & Sanderson 1975) and is complicated by the presence of numerous low-angle faults, mostly subparallel to both cleavage and bedding. Although many styles of boudinage occur in the region (including pinch-and-swell structure, internal boudinage and deformed tectonic, sedimentary and volcanic inclusions), our measurements are restricted to the boudinage of thin quartzite layers within the slates and phyllites which clearly originated by extension fracture. Boudins are, therefore, rectangular or sub-rectangular and subsequent separation of the boudins has left gaps filled both by matrix and by quartz crystallised from solution; examples are shown in Fig. 7. In all, we have measured eight layers containing a total of 91 boudins. All sections measured were within 10° of a well developed extension lineation; sections normal to this do not exhibit boudinage of the quartzite layers.

Initial comparisons

Figure 8 shows that the agreement between the Tintagel boudinage and the basic theory of stress transfer is not particularly good. In only three of the eight layers are the boudins contained within the predicted range; overall, 21% of the boudins fall outside the predicted limits and, in one layer, more than half the boudins do so. The most likely reason for these discrepancies is that, whereas the basic theory assumes homogeneous materials, natural rock systems are unlikely to be homogeneous. In the next section we therefore develop a more sophisticated model for stress-transfer boudinage. This model recognises that parameters such as tensile fracture strength and elastic moduli will vary from point to point throughout a rock mass, and that these variations will result in a distribution of critical lengths which, in turn, will control the distribution of boudin lengths. Model parameters and their distributions are based on the limited experimental data

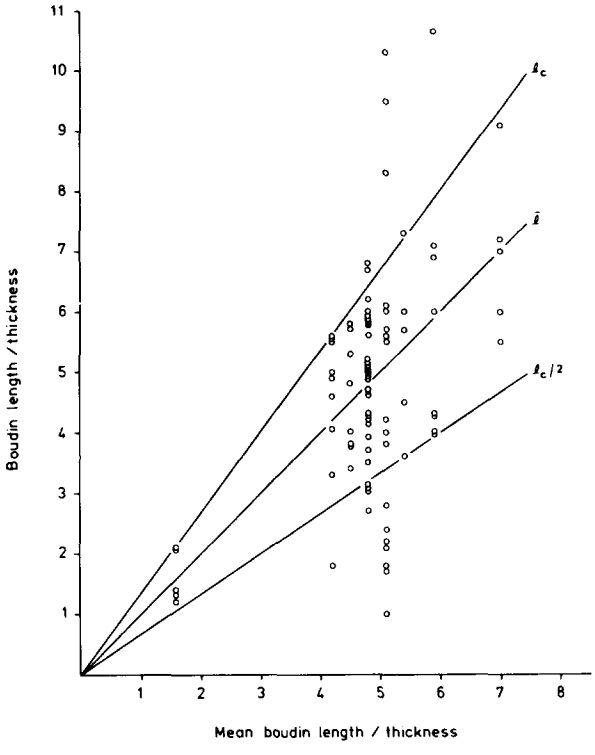

Fig. 8. Initial comparison of natural boudinage with stress-transfer theory. Ninety-one boudins on a plot of length/thickness vs mean length/thickness per layer; the lines marked l_c and $l_c/2$ are the upper and lower limits predicted by the stress-transfer theory (see text).

available for quartzite and slate, the critical length distributions being derived from these via the method of repeated sampling known as the Monte Carlo method (Ferguson & Harvey in press).

MATHEMATICAL BASIS OF THE MODIFIED STRESS-TRANSFER MODEL

Equation (5) shows that the maximum tensile stress in a layer occurs at its centre; we can therefore write

$$\sigma_{max} = \sigma_{|x=l/2} = E_s\varepsilon[1 - \text{sech}\ (\beta l/2)]. \qquad (18)$$

If the ultimate tensile strength of the layer is σ_{uf} the layer will fracture when $\sigma_{uf}/\sigma_{max} \leqq 1$. The condition $\sigma_{uf}/\sigma_{max} = 1$ therefore defines a local critical length (l_c) and so,

$$\frac{\sigma_{uf}}{E_s\varepsilon(1 - \text{sech}\ (\beta l_c/2)} = 1. \qquad (19)$$

It is reasonable to assume that the matrix strain, ε, remote from the layer will be determined by the mean values of σ_{uf}, E_s and G_m. For a prescribed l_c (say $l_c = z$) we can therefore calculate a value, ε^*, such that these mean values satisfy equation (19). Hence,

$$\varepsilon^* = \varepsilon_{|l_c=z} = \frac{\bar{\sigma}_{uf}}{\bar{E}_s[1 - \text{sech}\ (\bar{\beta}z/2)]} \qquad (20)$$

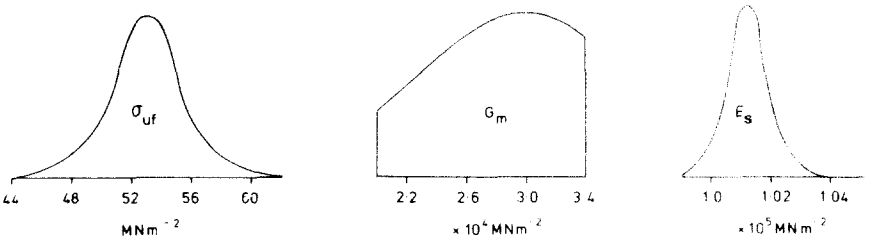

Fig. 9. Truncated normal distributions used in the Monte Carlo simulations: σ_{uf}, ultimate fracture stress; G_m, shear modulus of the matrix (slate); E_s, Young's modulus of the layer (quartzite).

in which, from equation (14),

$$\bar{\beta} = \left(\frac{\bar{G}_m}{\bar{E}_s(y - t/2)t}\right)^{1/2}, \tag{21}$$

the overbars denoting mean values.

Treating ε^* as a constant for a given value of z we can now select random values of σ_{uf}, E_s and G_m from appropriate distributions in order to calculate the corresponding random value of l_c. Thus we have,

$$f(l_c) = E_s\varepsilon^*(1 - \text{sech}\,[\beta l_c/2)]) - \sigma_{uf} = 0 \tag{22}$$

which leads to the Newton–Raphson formula,

$$(l_c)_{i+1} = (l_c)_i - \frac{1 - \text{sech}\,[\beta(l_c)_i/2] - \sigma_{uf}/E_s\varepsilon^*}{0.5\,\beta\,\text{sech}\,[\beta(l_c)_i/2]\,\tanh\,[\beta(l_c)_i/2]}. \tag{23}$$

where the starting value of l_c is the value z used to calculate ε^*.

The main input requirements for the model are, therefore, data on tensile fracture strength of quartzite (σ_{uf}), shear modulus of slate (G_m) and Young's modulus of quartzite (E_s); in each case a distribution of values is required rather than a single value. Due to the paucity of relevant experimental data deriving these distributions has proved to be the most difficult part of the study. The final distributions used are shown in Fig. 9, their derivation being discussed in detail in the Appendix. Throughout the simulations described in the next section the boudinaged layer is assumed to be 2 cm thick and the mean spacing between boudinaged layers is taken as 50 cm. These dimensions are appropriate to the scale of most of the Tintagel boudins.

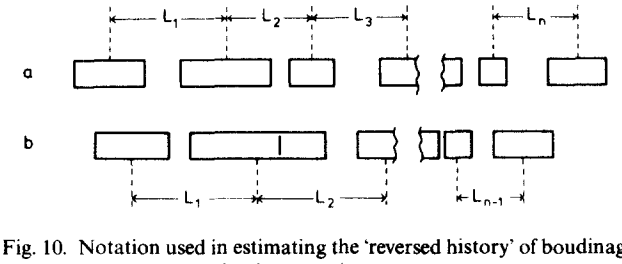

Fig. 10. Notation used in estimating the 'reversed history' of boudinage development (see text).

COMPUTER SIMULATIONS AND COMPARISON WITH TINTAGEL BOUDINAGE

There are three main steps involved in simulating a distribution of boudin lengths. These are: (1) calculation of random l_c values which take into account the distributed (rather than single-valued) nature of σ_{uf}, E_s and G_m; (2) a mid-point fracturing procedure and (3) repeated sampling to build up a distribution, followed by testing of the observed boudin distribution for goodness-of-fit to the simulated (predicted) distribution. These steps are now discussed in turn.

Random l_c values

This involves straightforward application of equation (23). That is, from each of the parameter distributions shown in Fig. 9, a random value is drawn using a normal pseudo-random number generator (Marsaglia *et al.* 1964). Equation (23) is then solved iteratively using a starting value of $(l_c)_i = z$ to yield the corresponding random value of l_c. Repeated application allows one to build up a distribution of l_c values to replace the single value which would correspond to the mean values of σ_{uf}, E_s and G_m.

Midpoint fracturing

It is easy to visualize the sequential break-up of an initial layer segment by midpoint fracturing until the fragments (boudins) are all of length $l < l_c$. For example, if we assume an initial layer segment of unit thickness and length 300, and a critical length of $l_c = 8$ then successive midpoint fractures will lead to length reduction according to 300 → 150 → ... → 9.375 → 4.6875. On the other hand, with an initial length of 250 we have 250 → 125 → ... → 15.625 → 7.8125. The large difference in final boudin length is because the 300 → sequence requires six successive midpoint fractures to ensure $l < l_c$ while the 250 → sequence requires only five. Even if l_c values are drawn from a distribution as outlined above, and the initial layer segments are also drawn from a distribution, this sample bisection effect can profoundly influence the final length distribution. Clearly our choice of initial layer segment length is not an arbitrary matter and must be determined in some way from the field data. Now, even in an undeformed sequence rock layers are not uniform and continuous for very large distances. They contain a

number of inbuilt major flaws (e.g. joints, sedimentary features, etc.) which we take to represent natural boundaries defining initial layer segments (e.g. Fig. 7d). If we simulate many such randomly located major flaws, the final length distribution of boudins after successive midpoint fracturing will contain more short boudins than if we simulate few. Indeed, if two major flaws happen to be separated by a distance $d < l_c$ then they immediately define a final boudin length, and if $d < l_c/2$ the boudin length will fall outside the range predicted by simple stress-transfer theory. It would of course be possible to choose (by trial and error) the number of flaws per unit length of layer that would optimize the fit between predicted and observed boudin length distributions; we prefer instead to determine an appropriate number of major flaws from careful analysis of our data on the Tintagel boudinage. This is made possible because our measurements include not only the aspect ratios of boudins but also their order within the boudinaged layer and the width of each inter-boudin gap.

We assume that boudinage development is a sequential 'fracture and separation' process so that, broadly speaking, large inter-boudin gaps correspond to early fracture sites and small gaps to later ones. A reversed history of boudinage development can, therefore, be derived as follows (see Ferguson 1981). A boudinage system, comprising $n + 1$ continuously exposed boudins in a single layer, is partitioned into subsystems of length L_i $(i = 1, n)$ as shown in Fig. 10(a). The system, in which for simplicity the boudins are treated as passive mechanical elements, is considered to shorten parallel to the layer in 0.5% increments; that is, the natural strain increment is ln (0.995). The steps in our procedure are then as follows: (1) Determine which subsystem requires the least number of shortening increments in order to reduce its inter-boudin gap to less than 1 mm (at which point the gap is considered to be closed); note this number of increments, S. (2) Apply S increments of shortening to each subsystem. (3) Relabel the subsystem lengths as shown in Fig. 10(b).

Steps (1)–(3) are then repeated until all inter-boudin gaps are closed, thus yielding a set of S values, S_i $(i = 1, n)$ corresponding to the n inter-boudin gaps.

This procedure has been applied to one of the Tintagel layers (layer 4, see Fig. 13) consisting of 33 boudins and its S-value histogram is shown in Fig. 11. We now argue that, because of the progressive shortening employed in our analysis, a layer devoid of major inbuilt flaws would yield a set of small S-values with rather little dispersion since most subsystems would be very similar. The S-value histogram for layer 4 shows this feature but also includes a small number of S-values that are distinctly larger than the rest. It seems reasonable to interpret these outlying values as representing major flaws or inbuilt fractures which allowed substantially greater amounts of separation away from these sites early in the extensional history of the layer. On this basis layer 4 contained at least four major flaws in an initial layer segment of length 2.76 m (the sum of the 33 boudin lengths). Unfortunately, the other layers measured at Tintagel contain too few boudins to warrant a similar analysis.

Our distribution of initial lengths is, therefore, set up by generating four random flaws from the uniform distribution between 0 and 276, thus defining five initial boudins. The analysis then proceeds with the computation of a random critical length as outlined earlier, successive bisection of the first initial boudin until its length is less than the critical length, and so on for the other four initial boudins. Thereafter four new initial flaws are generated in another 2.76 m layer segment and the procedure repeated until a suitable number of boudin lengths have been determined.

Comparison between predicted and observed boudin distributions

The steps outlined above are repeated 10,000 times (with a new random value of l_c each time) in order to build up a distribution of boudin lengths appropriate to the chosen value of z (which, in effect, determines the mean boudin length). Several such simulations, each of size 10,000, are performed using different values of z so that a set of cumulative probability curves are derived (Fig. 12). From each of these curves the boudin lengths defined by the 10th, 20th, ..., 90th percentiles ($l_{10}, l_{20}, \ldots l_{90}$) are read off and marked on the boudin length vs mean boudin length plot, their location on the abscissa being determined by the mean value $\bar{l}$,

$$\bar{l} = (l_{10} + l_{30} + l_{50} + l_{70} + l_{90})/5.$$

The sets of corresponding percentile points are then joined by smooth curves as shown in Fig. 13. Note that these curves do not yield a sharply-defined minimum boudin length. This is because two major flaws could be very close together so that very small boudin lengths are possible even though their probability is small.

A comparison between the predicted number of boudins falling in the intervals so determined and the observed numbers has been made and evaluated using the χ^2 goodness-of-fit test. The agreement (Table 1a) is close, the calculated χ^2 value being very much less than the critical probability of 0.05 with 9 degrees of freedom ($\chi^2 = 16.92$). Note that much of the discrepancy between observed and predicted numbers is in the low tail region; overall the agreement is very good but there are more small aspect ratio boudins than predicted. It is tempting to suggest that the fracture and separation analysis of layer 4 has led to

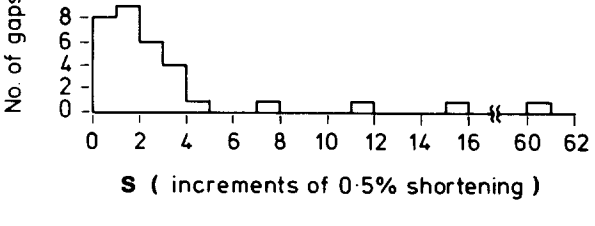

Fig. 11. S-value histogram for layer 4 at Tintagel. Each S-value used to construct the histogram is the number of increments of 0.5% shortening required to close an inter-boudin gap as shown in the model summarized in Fig. 10.

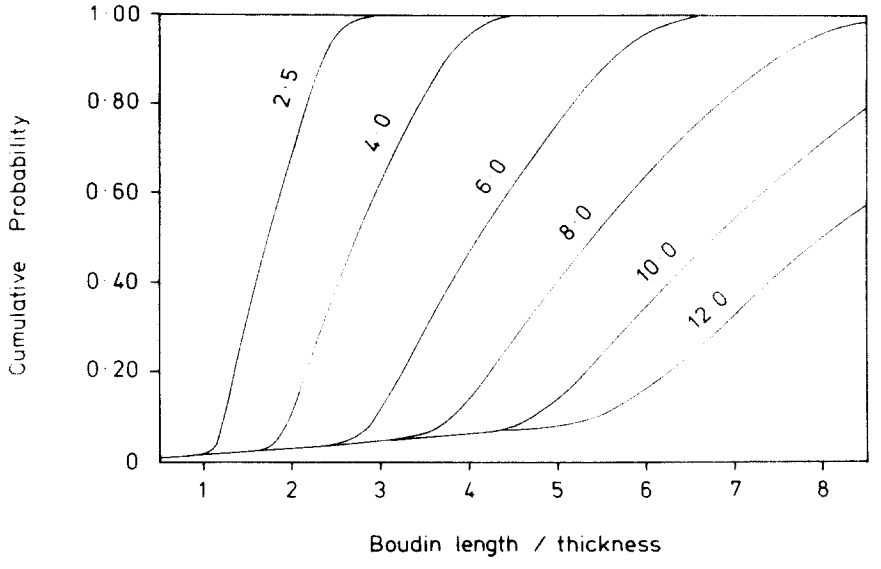

Fig. 12. Cumulative probability curves of boudin aspect ratios derived from the Monte Carlo simulations with inbuilt major flaws. Each curve is built up from 10,000 randomly generated boudin lengths (assuming that an initial layer segment of 2.76 m contains four initial flaws) and is labelled with the critical length, z, used in the simulation (see text and equations 20 and 23).

slight underestimation of the number of inbuilt major flaws. But let us first ask how layer 4 alone performs in the goodness-of-fit test. We cannot, of course, make the comparison using 10-percentile intervals because the χ^2 test requires a minimum expectation of five for each comparison interval. Using 20 per cent intervals (Table 1b) we see that the fit is excellent, the χ^2 value being very much less than the 95% confidence value with four degrees of freedom ($\chi^2 = 9.49$). Furthermore, the discrepancies are not concentrated in the smallest aspect-ratio interval. This suggests that had we been able to determine a number of inbuilt major flaws for each layer, the overall comparison between model predictions and observations would have been even better than that shown in Table 1(a).

Table 1. Chi-squared goodness-of-fit between the numbers of boudins occurring in the intervals marked on Fig. 13 and those predicted by the stress-transfer theory. (a) All ninety-one boudins; (b) thirty-three boudins in layer 4

	Percentile interval	Number observed	Number expected	χ^2
(a)	> 90	7	9.1	0.4846
	90–80	10.5	9.1	0.2154
	80–70	12.5	9.1	1.2703
	70–60	9	9.1	0.0011
	60–50	11	9.1	0.3967
	50–40	3	9.1	4.0890
	40–30	8.5	9.1	0.0396
	30–20	8	9.1	0.1330
	20–10	6.5	9.1	0.7429
	< 10	15	9.1	3.8253
				11.198
(b)	> 80	4.5	6.6	0.6682
	80–60	8	6.6	0.2970
	60–40	9.5	6.6	1.2742
	40–20	5.5	6.6	0.1833
	< 20	5.5	6.6	0.1833
				2.606

DISCUSSION

The boudin aspect-ratio distribution predicted by the stress-transfer model is impressively close to the observed distribution of boudins at Tintagel. It is important, therefore, to emphasize the special nature of the simulation developed in the previous sections. The model is, in a sense, statistical and yet we have made no attempt to select material properties and layer characteristics in order to maximize goodness-of-fit between the model predictions and the field measurements. The material properties used have been derived, directly or indirectly, from published experimental work on quartzite and slate. The inbuilt flaw properties of the simulated layers have been derived from analysis of the boudin length and gap length measurements collected in the field. The final agreement between the predictions of stress-transfer theory and the observed boudin aspect-ratio distribution therefore ranks as an important corroboration of the theory. But in interpreting this result we should be clear about the following two points: statistical significance and model generality.

Statistical significance

In setting up a chi-squared test we are proposing a hypothesized distribution of normalized boudin lengths. Stated rather formally, if the percentile intervals marked on Fig. 13 are labelled $i = 1, 2, \ldots, m$ and the total number of boudins measured is N, then we are testing the null hypothesis

$$H_o: n_i = N/m \text{ for all } i,$$

where n_i is the number of boudins in the ith percentile interval, against the alternative hypothesis

$$H_1: \text{the } n_i \text{ do not have this distribution.}$$

In choosing a critical probability of 0.05 we are specifying

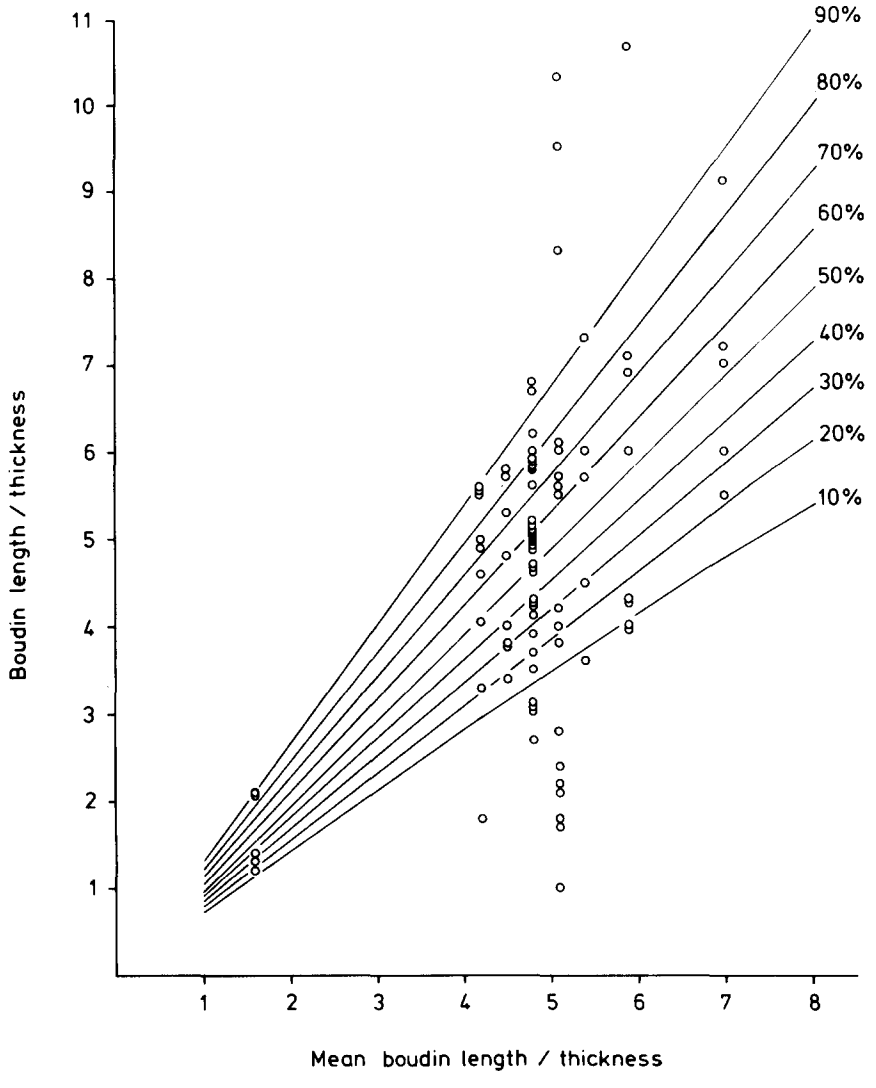

Fig. 13. Ninety-one boudins at Tintagel on a plot of aspect ratio vs mean aspect ratio per layer. The curves are constructed using percentiles (as indicated) read off the probability curve of Fig. 12. The 'layer 4' referred to in the text is the fourth set of boudins counting from the left (i.e. with a mean length/thickness of 4.8).

an acceptable probability of rejecting H_o when it is in fact true. But we are really interested in the probability of accepting H_o even though it is false. It is important to be clear, then, that in spite of the excellent fit of theory to data, this tells us nothing very specific about our probability of wrongly accepting the stress-transfer theory. But it does tell us something, as the following thought experiment shows. Let us imagine that a population of boudins exists somewhere that developed exactly according to the stress-transfer theory; we will call this a population of ideal stress-transfer boudins. If we then take many samples of 91 boudins from this ideal population, plot them on the diagram (i.e. Fig. 13) and perform the chi-squared test (as in Table 1a) then the χ^2 values would vary about a mean (expected) value, μ, of 9 because in a chi-squared distribution $\mu = \nu$, where ν is the number of degrees of freedom. Similarly, using 20-per cent intervals (Table 1b) with samples of 33, the mean value of many chi-squared tests would be 4.

Now the fit obtained with the layer 4 data is actually closer to a perfect fit to the stress-transfer prediction than the fit expected with 'ideal stress-transfer' boudins as it yields as χ^2 value below the expected value. Of course we should not make too much of this value being below the expected fit for ideal boudins as values above or below the mean would be equally likely. The point is that 'ideal' boudins could hardly be expected to perform better in the chi-squared test than the Tintagel boudins actually do perform. Or, stated another way, if we knew the true model (i.e. that which controlled in every detail the exact development of the Tintagel boudins) we could not expect a better goodness-of-fit to the true model than we actually get to the stress-transfer model. In short, with a sample of one (albeit composed of 91 boudins) the chi-squared test would in effect be unable to discriminate between the true model and the stress-transfer model. Further progress therefore depends firstly on much more field data. Secondly, only when specific alternative models are proposed can we calculate the probability of wrongly accepting the stress-transfer theory relative to the specific alternative. We hope that field geologists and theoreticians alike will take up this challenge.

Generality of the model

At first sight it may seem that the stress-transfer model proposed in this paper is very specific, especially as we have gone to some considerable trouble to estimate distributions for σ_{uf}, E_s and G_m appropriate to the Tintagel lithologies. But it must be remembered that we do not know *a priori* the critical length, l_c, which controls the boudin bisection process. We calculate what the dispersion of boudin aspect ratios would be for a variety of postulated l_c ($= z$) values as shown in Fig. 12. Had we chosen very different mean values for σ_{uf}, E_s and G_m the dispersion of aspect ratios for a given z would be essentially the same, although the ε^* value which controls the stress-transfer would be different. In short, the dispersion of aspect ratios is controlled by the dispersion of σ_{uf}, E_s and G_m, not by the mean values of these parameters. The basic model could therefore be applied unchanged for other rock types so long as the shapes of the σ_{uf} and E_s distributions for the boudin lithology are (or are assumed to be) similar to those for quartzite, and similarly for the shape of the G_m distribution for the matrix lithology.

In another sense the model is very specific in that the cumulative curves of aspect ratio (Fig. 12) are markedly dependent on the incidence of major inbuilt flaws, and this we have estimated directly from the Tintagel field data. However, we can easily produce new sets of curves corresponding to different inbuilt flaw densities.

Implications of the stress-transfer model for layer boudinage

In the stress-transfer model, extension fracturing is a sequential process. Although we have used an elastic fracture mechanics approach, some natural fracture boudinage may be controlled by elastic–plastic fracture (Lloyd & Ferguson 1981) leading to boudin shapes other than ideal rectangular forms. At any instant during boudinage different parts of an originally continuous layer may be responding by fracture, by locally plastic deformation, or by boudin separation. Structures in the nearby matrix will be correspondingly varied. Inter-boudin gaps will not be of equal length and hence any strain estimation based on comparing initial and final layer lengths will depend on which part and how much of a layer is sampled (Fig. 14). Ferguson (1981) demonstrated that the strain estimate will depend also on the timing of the fracture sequence so that two layer segments having the same initial and final lengths need not have suffered the same amount of extension (Fig. 15). Some of these strain-estimation problems can be partly overcome by using a strain reversal technique (Ferguson 1981) which makes an estimate of the strain due to inhomogeneous matrix flow as well as that due to boudin separation. This approach substantially improves the accuracy of strain estimates based on boudinage; but because matrix strain occurring before the first fracture appeared in a layer segment will be unrecorded, any boudinage strain estimate will be less than the matrix strain which would have occurred had the boudinaged layer been absent.

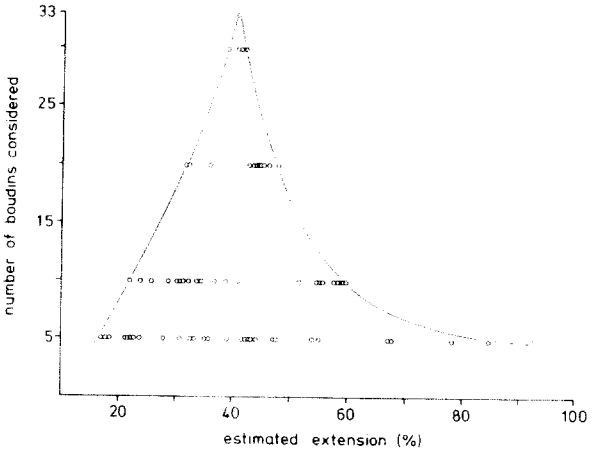

Fig. 14. Variation in finite strain estimate depending on which part and how much of a layer is considered; layer 4 at Tintagel (see caption to Fig. 13) comprising 33 boudins. With 33 boudins there are 29 possible subsets of five adjacent boudins, and strain estimates using these subsets range from about 12% to over 90% extension. The 24 possible subsets of ten adjacent boudins yield strain estimates ranging from about 22% to 61% extension, and so on. Extension, e, is standard using $e = [\Sigma \text{(boudin + gap length)} - \Sigma \text{(boudin length)}]/\Sigma \text{(boudin length)}$.

Since, in a stress-transfer process, early fractures influence the location of subsequent fractures, the resulting boudinage cannot be a random structure. The sequential fracture development suggests that extension-fracture boudinage should be a periodic structure of the saturation type (Cobbold & Ferguson 1979). However, Fig. 13 shows that, as the mean aspect ratio of boudins per layer increases, the range of individual aspect ratios increases leading to an apparent decrease in regularity; there is a greater probability of boudins having a wide range of aspect ratios while remaining within the framework of the stress transfer model.

Finally, we pointed out earlier that the range of boudin aspect ratios predicted by stress transfer theory depends on the dispersion of material properties (σ_{uf}, E_s, G_m) rather than on the mean values. It should be clear, however, that if the mean values used correspond fairly closely to those controlling natural boudinage then very little further analysis is needed to derive a palaeostress estimate from boudinage structure. We develop this idea in another paper (Ferguson & Lloyd in press) in which we use the Tintagel boudinage to provide constraints on the evolution of a major overfold at the southern margin of the Culm Synclinorium, SW England.

Extension fracture of brittle minerals and fossils

We commented earlier on recent fibre-loading-type interpretations of mineral fracturing in some mylonites (White *et al.* 1980, Watts & Williams 1980, Boullier 1980). The question now arises whether the Kelly theory or our modification is the more appropriate model for such cases. Of course, except for geometric considerations, the two models are very similar. Ideally, then, the geometry

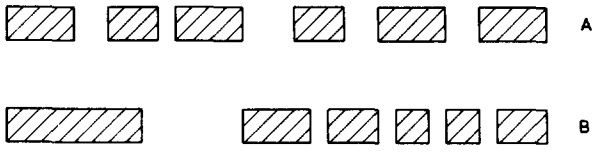

Fig. 15. Two inclusion fragment trains having the same initial length (L_i = sum of fragment lengths) and final length (L_f = sum of fragment lengths and gap lengths). Using $e = (L_f - L_i)/L_i$ the extension estimate is 45.5% but using the strain reversal method of Ferguson (1981) train B records more far-field extension (67.2%) than train A (56.2%).

dependent features in our analysis should be derived for the relevant mineral morphology. In practice, we believe that the fibre loading analysis should provide a good approximation for prismatic minerals while our layer–matrix theory is probably better for feldspars, especially if {010} is well developed. Thereafter, our simulation approach incorporating distributed parameters should be used although some simplifications may be possible, especially for boudinage of one material within another (e.g. rutile needles within quartz). We hope to report our work on mineral and fossil boudinage in a future paper.

One aspect is worth developing here however. The fibre loading/stress-transfer model predicts that the presence of brittle minerals will enhance ductile deformation in the nearby matrix because the mineral terminations act as stress raisers. As a mineral becomes disrupted by successive fractures the extra terminations formed will further enhance local ductility. Tewary (1978) has argued that, during fibre-loading deformation, a fibre composite may therefore exhibit an increase in overall ductility. Mitra (1978) has argued similarly for some mylonites although he attributed fracturing to dislocation pile-ups at obstacles along the mineral–matrix boundary. For some alloys, Adam & Eady (1979) showed that a comparable process may have far reaching consequences because fibre fracturing acts as a source for dislocation tangles. These may extend from fibre to fibre eventually forming dislocation networks and cells which lead to polygonisation and grain refinement. It is therefore worth emphasizing that, although our main concern in this paper is with layer boudinage, the stress transfer model may have considerable relevance to microstructure development in some tectonites.

CONCLUSIONS

(1) The theory of fibre loading developed to explain the behaviour of fibre composite systems can be adapted for extension fracture of layer–matrix systems provided that the relevant geometric expressions are rederived. The behaviour of layer–matrix systems in extension depends on the nature of the stress transfer between matrix and layer.

(2) The stress-transfer theory predicts that maximum tensile stress occurs midway between layer segment ends. This controls the most likely position of any subsequent fracture provided that the maximum tensile stress in the layer segment exceeds the ultimate failure strength of the layer. There is, therefore, a critical layer length below which further fracture cannot occur.

(3) Maximum values of shear stress occur at the ends of layer segments, which act as local stress raisers promoting ductile deformation in the matrix.

(4) Elastic–plastic finite-element simulations of extension-fracture boudinage are in close agreement with the predictions of the stress-transfer theory.

(5) Realistic application of stress-transfer theory to natural extension-fracture boudinage depends on the recognition that, in nature, parameters such as the ultimate failure stress, layer Young's modulus and matrix shear modulus, will vary from point to point. The dispersion of these parameters is important in controlling the dispersion of boudin aspect ratios.

(6) Natural rock layers are likely to contain randomly distributed inbuilt flaws. The number of such flaws per unit length of layer can be estimated by recognizing that, in any stress transfer mechanism, the largest gaps correspond to the earliest fracture sites. Therefore, very large gaps probably represent the sites of initial flaws.

(7) Incorporation of distributed parameters and initial flaws into the basic stress transfer model results in very close agreement between predicted boudin aspect ratios and those observed in examples of natural boudinage from Tintagel, Cornwall.

(8) Extension-fracture boudinage which develops by a stress-transfer process may involve simultaneous fracture, separations and local ductile deformation at different positions in a layer.

(9) By recognizing the sequential nature of fracturing implied in the stress-transfer model, an improved method for estimating finite strain from boudinage structure can be derived. In some circumstances palaeostress estimates are also possible.

(10) The fracture of mineral grains by a stress-transfer type mechanism may be important in controlling the development of microstructure in some tectonites, especially mylonites.

Acknowledgements—We thank Stan White, Graham Williams and Mike Watts for valuable discussions during the early stages of this work. Fieldwork was supported by a University of Nottingham postgraduate studentship to G.E.L. Facilities for computing, and manuscript and diagram preparation were provided by the Department of Geology, University of Nottingham.

REFERENCES

Adam, C. M. & Eady, J. A. 1979. The deformation behaviour of Al–Al_6 Fe eutectic alloys. *Acta metall.* **27**, 79–87.

Agarwal, B. D., Lifshitz, J. M. & Broutman, L. J. 1974. Elastic–plastic finite element analysis of short-fibre composites. *Fibre Sci. Technol.* **7**, 45–62.

Allison, I. & Latour, T. E. 1977. Brittle deformation of hornblende in a mylonite. *Can. J. Earth Sci.* **14**, 1953–1958.

Atkinson, B. K. 1979a. A fracture mechanics study of subcritical tensile cracking of quartz in wet environments. *Pure appl. Geophys.* **117**, 1011–1024.

Atkinson, B. K. 1979b. Fracture toughness of Tennessee Sandstone and Carrara Marble using the double torsion testing method. *Int. J. Rock. Mech. Min. Sci. Geomech. Abstr.* **16,** 49–53.
Atkinson, B. K. 1980. Stress corrosion and rate-dependent tensile failure of a fine-grained quartz rock. *Tectonophysics* **65,** 281–290.
Birch, F. 1966. Compressibility and elastic constants. In: *Handbook of Physical Constants* (edited by Clark, S. P.), *Mem. geol. Soc. Am.* **97,** 97–173.
Boullier, A. M. 1980. A preliminary study of the behaviour of brittle minerals in a ductile matrix: example of zircons and feldspars. *J. Struct. Geol.* **2,** 211–217.
Brace, W. F. 1964. Brittle fracture of rocks. In: *State of Stress in the Earth's Crust* (edited by Judd, W. R.) American Elsevier Publishing Co. New York, 111–124.
Brown, W. F. Jr. & Srawley, J. E. 1966. *Plane Strain Crack Toughness Testing of High Strength Metallic Materials.* ASTM STP 410, American Society for Testing and Materials.
Cloos, E. 1947. Boudinage. *Trans. Am. geophys. Un.* **28,** 626–632.
Cobbold, P. R., Cosgrove, J. W. & Summers, J. M. 1971. Development of internal instabilities in deformed anisotropic rocks. *Tectonophysics* **12,** 23–53.
Cobbold, P. R. & Ferguson, C. C. 1979. Description and origin of spatial periodicity in tectonic structures: report on a Tectonic Studies Group conference held at Nottingham University, 8 November 1978. *J. Struct. Geol.* **1,** 93–97.
Cox, H. L. 1952. The elasticity and strength of paper and other fibrous materials. *Br. J. appl. Phys.* **3,** 72–79.
Davidge, R. W. 1980. Combination of fracture mechanics, probability and micromechanical models of crack growth in ceramic systems. *Metal Sci. J.* **14,** 459–462.
Ekstrom, T. K. 1975. Pinch and swell structure from a Swedish locality *Geol. För. Stockh. Förh.* **97,** 180–187.
Ferguson, C. C. 1981. A strain reversal method for estimating extension from fragmented rigid inclusions. *Tectonophysics* **79,** T43–T52.
Ferguson, C. C. & Harvey, P. K. (in press). The Monte Carlo method: a brief review and some applications in metamorphic petrology *Misc. Pap. geol. Soc. Lond.* **14.**
Ferguson, C. C. & Lloyd, G. E. (in press). Palaeostress and strain estimates from boudinage structure and their bearing on the evolution of a major Variscan fold-thrust complex in southwest England. *Tectonophysics.*
Freshney, E. C., McKeown, M. C. & Williams, M. 1972. Geology of the coast between Tintagel and Bude. *Mem. geol. Surv. (U.K.).*
Fullagar, P. K. 1980. A description of nucleation of folds and boudins in terms of vorticity. *Tectonophysics* **65,** 39–55.
Gay, N. C. & Jaeger, J. C. 1975. Cataclastic deformation of geological materials in matrices of differing composition: II Boudinage. *Tectonophysics* **27,** 323–339.
Griggs, D. T. & Handin, J. 1960. Observations on fracture and a hypothesis of earthquakes. In: *Rock Deformation (A Symposium).* (edited by Griggs D. T. & Handin J.) *Mem. Geol. Soc. Am.* **79,** 347–364.
Hayes, D. J. 1978. Origins of the stress intensity factor approach to fracture. In: *A General Introduction to Fracture Mechanics* (J. Strain Anal. Monogr.), Mechanical Engineering Publications Ltd., London, 9–16.
Henry, J.-P. & Paquet, J. 1976. Mechanique de la rupture des roches calcitiques. *Bull. Soc. géol. Fr.* **18,** 1573–1582.
Hobson, D. M. & Sanderson, D. J. 1975. Major early folds at the southern margin of the Culm Synclinorium. *J. geol. Soc. Lond.* **131,** 337–352.
Irwin, G. R. 1960. Plastic zone near a crack and fracture toughness. *Proc. 7th Sagamore Ordnance Materials Research Conf.*, Rpt. No. MeTE 661/661/F, Syracuse Univ. Research Inst.
Kelly, A. 1973. *Strong Solids.* Clarendon Press, Oxford.
Knott, J. F. 1973. *Fundamentals of Fracture Mechanics.* Butterworths, London.
Lloyd, G. E. & Ferguson, C. C. 1981. Boudinage structure — some new interpretations based on elastic–plastic finite element simulations. *J. Struct. Geol.* **3,** 117–128.
Lohest, M. 1909. De l'origine des veins et des geodes des terrains primaires de Belgique. *Annls Soc. géol. Belg.* **36,** 275–281.
Marsagalia, G., MacLaren, M. D. & Bray, T. A. 1964. A fast procedure for generating normal random variables. *Communs Ass. comput. Mach.* **7,** 4–10.
McKeown, M. C., Edmonds, E. A., Williams, M., Freshney, E. C. & Masson-Smith, D. J. 1973. *Geology of the country around Boscastle and Holsworthy* (explanation of sheets 322 and 323), *Mem. geol. Surv. U.K.*
Mitra, G. 1978. Ductile deformation zones and mylonites: the mechanical processes involved in the deformation of crystalline basement rocks. *Am. J. Sci.* **278,** 1057–1084.
Ohsawa, T., Nakayama, A., Miwa, M. & Hasegawa, A. 1978. Temperature dependence of critical fibre length for glass fibre reinforced thermosetting resins. *J. appl. Polymer Sci.* **22,** 3203–3212.
Paris, P. C. & Sih, G. 1964. Stress analysis of cracks. In: *Fracture Toughness Testing and its Application,* ASTM STP 381, Am. Soc. for Testing and Materials, 31–81.
Platt, J. P. & Vissers, R. L. M. 1980. Extensional structures in anisotropic rocks. *J. Struct. Geol.* **2,** 397–410.
Ramberg, H. 1955. Natural and experimental boudinage and pinch and swell structures *J. Geol.* **63,** 512–526.
Ramsay, J. G. 1967. *Folding and Fracturing of Rocks.* McGraw-Hill, New York.
Sahu, B. K. 1976. Mathematical theory of counting two-dimensional grains by line and ribbon methods. *Sediment. Geol.* **16,** 177–192.
Saltikov, S. A. 1967. The determination of the size distribution of particles in an opaque material from a measurement of the size distribution of their sections. In: *Stereology: Proc. Second Int. Cong. for Stereology* (edited by Elias, H.), Springer, New York, 163–173.
Sanderson, D. J. & Dearman, W. R. 1973. Structural zones of the Variscan fold belt in S.W. England, their location and development. *J. geol. Soc. Lond.* **129,** 527–533.
Sanderson, D. J. & Meneilly, A. W. 1981. Analysis of three-dimensional strain modified uniform distributions: andalusite fabrics from a granite aureole. *J. Struct. Geol.* **3,** 109–116.
Schwerdtner, W. M. 1970. Distributions of longitudinal finite strain in lenticular boudins and bending folds. *Tectonophysics* **9,** 537–545.
Selkman, S. 1978. Stress and displacement analysis of boudinages by finite element method. *Tectonophysics* **44,** 115–139.
Simmons, G. & Wang, H. 1971. *Single Crystal Elastic Constants and Calculated Aggregate Properties.* M. I. T. Press, Massachusetts, U.S.A.
Smith, R. B. 1975. Unified theory of the onset of folding, boudinage and mullion structure. *Bull. geol. Soc. Am.* **86,** 1601–1609.
Smith, R. B. 1977. Formation of folds, boudinage and mullions in non-Newtonian materials. *Bull. geol. Soc. Am.* **88,** 312–320.
Smith, R. B. 1979. The folding of a strongly non-Newtonian layer. *Am. J. Sci.* **279,** 272–287.
Stephansson, O. 1973. The solution of some problems in structural geology by means of the finite element technique. *Geol. För. Stokh. Förh.* **95,** 51–59.
Stephansson, O. & Berner, H. 1971. The finite element method in tectonic processes. *Phys. Earth Planet. Interiors* **4,** 301–321.
Strömgård, K.-E. 1973. Stress distribution during formation of boudinage and pressure shadows. *Tectonophysics* **16,** 215–248.
Talbot, C. J. 1970. The minimum strain ellipsoid using quartz veins. *Tectonophysics* **9,** 47–76.
Tewary, V. K. 1978. *Mechanics of Fibre Composites.* Wiley Eastern Ltd., New Delhi.
Troeng, B. 1975. One natural and some experimental pinch and swell structures. *Geol. För. Stockh. Förh.* **97,** 383–386.
Uemura, T. 1965. Tectonic analysis of the boudin structure in the Muro group, Kii peninsula, southwest Japan. *J. Earth Sci.* **13,** 99–114.
Watts, M. J. & Williams, G. D. 1980. Strain history of a mylonite (abstract). *J. Struct. Geol.* **1,** 338.
White, S. H., Burrows, S. E., Carreras, J., Shaw, N. D. & Humphreys, F. J. 1980. Mylonite development in ductile shear zones. *J. Struct. Geol.* **2,** 175–187.
Wilson, G. 1951. The tectonics of the Tintagel area, North Cornwall. *Q. Jl geol. Soc. Lond.* **106,** 393–432.
Wilson, G. 1961. Tectonic significance of small scale structures and their importance to geologists in the field. *Annls Soc. géol. Belg.* **84,** 423–549.

APPENDIX: ESTIMATION OF INPUT DISTRIBUTIONS FOR USE IN THE MONTE CARLO SIMULATIONS

Tensile fracture strength, σ_{uf}

There is hardly any relevant data on the fracture strength of quartzite in extension. In any case, tensile strength may be dependent on specimen dimensions and is not, therefore, a material property. It seems safer to arrive at a distribution of σ_{uf} via data on the critical stress intensity factor, K_{Ic}, for mode I (tensile) crack propagation, which is a material property. The two are related by an equation of the general form

$$K_{Ic} = \sigma_{uf} a^{1/2} Y, \tag{24}$$

Table 2. Relative K_{Ic} dispersion values for different materials

Material	Test method	Scaled S.D.	Source
Arkansas Novaculite	3PB	0.075	Atkinson 1980
Quartz (a plane $\perp z$)	DT	0.071	Atkinson 1979a
" (a plane $\perp r$)	DT	0.064	"
Micrites:			
Fallerans ($\eta = 2.1$)	3PB	0.078	Henry & Paquet 1976
" ($\eta = 2.6$)	"	0.077	"
" ($\eta = 3.7$)	"	0.064	"
D'etalans	"	0.115	"
La Vis	"	0.018	"
Muret le Chateau	"	0.099	"
Carrara Marble	DT	0.044	Atkinson 1979b
Tennessee Sandstone	DT	0.049	"
Steel	3PB	0.061	Knott 1973 Fig. 5.26
	CT	0.058	"
Aluminium alloy	3PB	0.092	"
	CT	0.100	"

Test methods are 3PB, three point bend; DT, double torsion; CT, compact tension. η is percentage total porosity. Scaled S.D. is the sample standard deviation multiplied by the ratio (sample mean)/(Arkansas Novaculite sample mean).

where a is a measure of crack size and Y is a calibration factor related to loading geometry, crack configuration and specimen dimensions (see Hayes 1978). Unfortunately there are few data on K_{Ic} for quartzite and virtually no reliable data for both tensile strength and K_{Ic} from which a critical crack length could be estimated. The situation is further complicated by microstructural considerations. For example, the surface energy requirement for a 'grain-size' crack should approximate to the cleavage or grain-boundary surface energy, but the effective surface energy for macroscopic fracture is usually an order of magnitude or more greater. This is because subcritical crack growth precedes catastrophic failure, the effective surface energy γ_i rising as the crack extends until failure occurs at a maximum value of γ_i/a at which the crack length, a, may be several grain diameters (Davidge 1980). This point can be illustrated using fracture mechanics data of Atkinson (1980) on fine grained quartzite (Arkansas Novaculite) fractured in three-point bend tests. For this geometry the critical stress intensity factor is related to failure stress through equation (24) in which

$$Y = 1.93 - 3.07(a/W) + 14.53(a/W)^2 - 25.11(a/W)^3 + \ldots .$$

In this calibration (Brown & Srawley 1966), W is the specimen depth. The experimental results of Atkinson ($\sigma_{uf} = 70\,\mathrm{MNm^{-2}}$; $K_{Ic} = 1.335\,\mathrm{MNm^{-3/2}}$) are satisfied when $a = 97\,\mu\mathrm{m}$, which is about 10 grain diameters. These data are not directly relevant to this study because the Novaculite is very fine grained and the experiments were conducted at atmospheric pressure. It is known that K_{Ic} for coarser-grained quartzites is usually about $1.5\,\mathrm{MNm^{-3/2}}$ (B. K. Atkinson, personal communication 1980) and is likely to increase with increasing confining pressure. We will therefore estimate K_{Ic} using the experimental data of Brace (1964).

Brace's experiments on extension failure of shaped ('dog-bone') specimens of Cheshire quartzite at $60\,\mathrm{MNm^{-2}}$ confining pressure yielded a tensile strength of $28\,\mathrm{MNm^{-2}}$. There are no data on stress intensity factors for this rock. However, if we assume that the critical flaw is an axially symmetric circular crack located within the specimen normal to the extension direction and that the effects of the specimen boundary surfaces on the stress field of the crack are negligible, then this geometry leads to the calibration factor $Y = 2/\sqrt{\pi}$ in equation (24) (Paris & Sih 1964, p. 39), in which a should be interpreted as the crack radius. We now postulate that critical flaw size will be related to microstructure in the same way as for Arkansas Novaculite. The mean grain size of Cheshire quartzite is 300 μm and, taking the critical crack dimension to be ten times this length (as in the Novaculite), equation (24) yields a value of $K_{Ic} = 1.73\,\mathrm{MNm^{-3/2}}$.

Our concern here is not to estimate a single value of σ_{uf} but a distribution of values. It would be logical to estimate this through a fixed value of K_{Ic} and a statistical description of critical flaw size, but no such data on flaw size exist. However, Atkinson (1980) has published data on the dispersion of K_{Ic} values for Arkansas Novaculite. For the purpose of the model, then, we will treat the critical flaw size as a contrast (to be estimated from the microstructure) and we will assume that the dispersion of K_{Ic} values (which presumably reflects local microstructural variations) is similar to that for the Novaculite. On this basis we have $K_{Ic} = 1.73$ with a standard deviation of 0.097. It may seem difficult to justify using a K_{Ic} dispersion value for only one rock as a guide to that expected in another. However, the dispersion values for widely different materials, when scaled to the Novaculite sample mean, are mostly close to Atkinson's Novaculite value (Table 2). This suggests that, in homogeneous materials, wide variations in K_{Ic} dispersions are unlikely.

The critical flaw size estimate is based on measurement of 200 grain diameters in a typical boudinaged quartz layer from Tintagel. The size analysis was complicated by the presence of larger statically (?) recrystallised grains which, so far as they could be identified, were excluded. After correction for grain count bias (Sahu 1976) and cut-effect (Saltikov 1967) the analysis yields a mean grain size of 84 μm. The critical

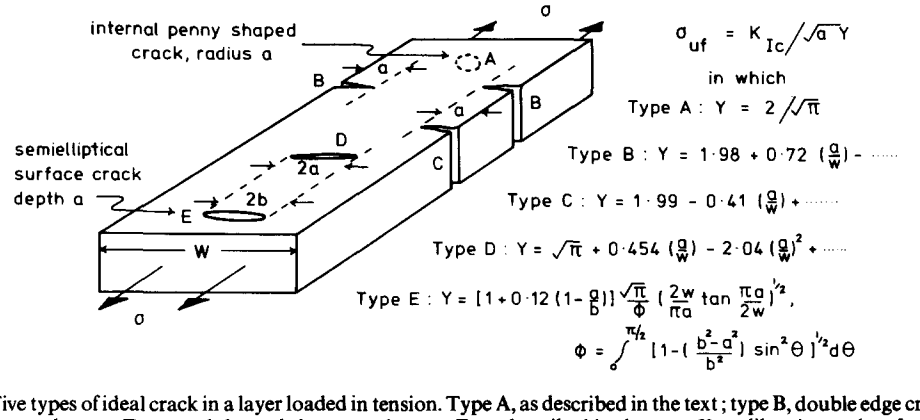

Fig. 16. Five types of ideal crack in a layer loaded in tension. Type A, as described in the text; type B, double edge crack; type C, single edge crack; type D, central through-layer crack; type E, as described in the text. K_{Ic} calibrations taken from Brown & Srawley (1964).

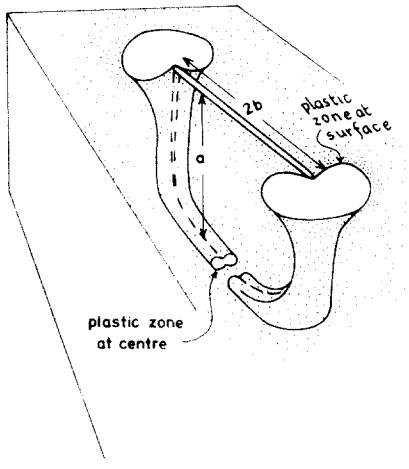

Fig. 17. Representation of plastic zone ahead of a mode I elliptical surface crack shows greater plasticity (greater toughness) at surface than at centre of layer.

flaw size has, therefore, been estimated as 840 μm in accordance with the grain size–critical flaw size relationship suggested by the Novaculite data.

We now need to use the K_{Ic} distribution and the critical flaw size estimate to derive a fracture strength distribution. Figure 16 shows five model crack configurations and their K_{Ic} calibrations. For natural boudinage it seems reasonable to assume that the width, w, of a layer will be orders of magnitude greater than the crack length so that only the first term in the calibration for crack types B, C and D need be retained. Similarly the tangent factor in crack type D reduces to 1 because w is very much greater than the crack depth. In choosing between these five models we argue that our assumption of $w \gg a$ for natural boudinage suggests that few free edges (pre-existing cracks?) would be present so that we expect very few microcracks of types B and C. A through-layer centre crack (type D) also seems implausible because this would presumably initiate either as an internal crack similar to type A or as a surface crack similar to type E. In either case we would expect the characteristic crack dimension, a, to reach its critical size before the crack extends through the thickness of the layer. The most likely crack types are, therefore, A and E. For type E we have the limiting calibrations,

$$\text{long shallow crack, } b/a \text{ large:} \qquad Y = 1.12\sqrt{\pi}$$

$$\text{deep (semicircular) crack, } b/a = 1\text{:} \quad Y = 2/\sqrt{\pi}.$$

Note that the semicircular surface crack has the same K_I calibration as the internal (type A) crack, while the long shallow surface crack has the same calibration as the through-layer centre crack (type D) except for the factor 1.12. This factor is a measure of the increased fracture toughness near the free surface which, in turn, is due to the increased size of the crack-tip plastic zone as conditions change from plane strain (at the centre) to more nearly plane stress at the surface (Fig. 17). Consequently we would expect slow crack extension to proceed more easily into the layer thus reducing the ratio b/a. So long as $b/a \simeq 1$ at failure the K_{Ic} calibration for crack Types A and E will be the same and we will therefore derive our distribution of fracture strength using

$$\sigma_{uf} = \sqrt{\pi}\, K_{Ic}/2\sqrt{a}. \tag{25}$$

This leads to a distribution with $\bar{\sigma}_{uf} = 52.9\ \mathrm{MNm}^{-2}$ and a standard deviation of 2.57.

Finally we should mention that, strictly, a in equation (25) is an effective crack dimension which may be larger than the actual dimension by an amount $(K_{Ic}/\sigma_y)^2/6\pi$ where σ_y is the yield strength. This amount is Irwin's (1960) estimate of the correction necessary for matching an elastic–plastic crack to an equivalent elastic crack in plane strain. Because a is large relative to $(K_{Ic}/\sigma_y)^2$ we will ignore this correction (with $\sigma_y = 100\ \mathrm{MNm}^{-2}$ the correction would reduce σ_{uf} by only about 1%). It should be remembered, though, that if fast fracture takes place near the yield point, neglecting this term may introduce appreciable relative errors if the critical flaw size is small. Note also that some workers introduce a multiplying factor of $(1 - \nu^2)^{-1/2}$ into the K_{Ic} calibrations (which are essentially two dimensional) in order to improve their accuracy for real plane strain conditions. For quartzite (Poisson's ratio $\nu \simeq 0.1$) this correction is also negligible.

Shear modulus of matrix, G_m

The slate matrix surrounding the boudinaged quartzite layers at Tintagel is of very variable character in thin section. The predominant very fine grained white mica–quartz assemblage shows many small-scale variations including graphite-rich layers, quartz lenses, coarser white mica lenses, and occasional calcite. We know of no experimental data on the dispersion of G values for any single slate. In any case, samples for experimental determination of elastic moduli are usually selected for their homogeneity, and dispersion data would be unlikely to reflect the very heterogeneous response expected in a matrix as variable as the Tintagel slates. Therefore, in order to provide data for the simulations, we have taken data for a variety of slates and schists (Birch 1966) in the hope that the statistical measures derived from a set of different rocks will reflect the within-rock variations of a single very inhomogeneous slate. This procedure yields $\bar{G}_m = 2.99 \times 10^4\ \mathrm{MNm}^{-2}$ with a standard deviation of 0.73×10^4.

Young's modulus of layer, E_s

We have used the mean and standard deviation derived from ten determinations for quartz aggregates (Voight averaged) taken from Simons & Wang (1971); namely $1.012 \times 10^5\ \mathrm{MNm}^{-2}$ with a standard deviation of 6.9×10^2.

Truncation of distributions

A problem with Monte Carlo computer simulations in which values are drawn randomly from normal distributions is that, with large simulations, it is possible to draw extreme values that fall outside the limits of the solution set determined by the fixed parameters. The normal distributions for σ_{uf}, G_m and E_s have therefore been truncated to avoid this problem (see Fig. 9). The upper limit for G_m, $3.4 \times 10^4\ \mathrm{MNm}^{-2}$, is chosen because values much larger than $E_s/3$ seem unreasonable. The lower limit, $2.1 \times 10^4\ \mathrm{MNm}^{-2}$, is chosen to avoid values much smaller than the lowest value in the compilation of Birch (1966). Truncation of the normal distributions for σ_{uf} and E_s exclude only a tiny fraction of the total areas beneath the curves; the limits chosen are $\pm$ 3S where S is the standard deviation.